Chinese Chemical Letters 32 (2021) 2427–2432

Contents lists available at ScienceDirect

Chinese Chemical Letters

journal homepage: www.elsevier.com/locate/cclet

Communication

Cu/Cu_2O nanoparticles co-regulated carbon catalyst for alkaline Al-air batteries

Jing Tian[a], Depei Liu[b], Jingsha Li[a,c], Dan Sun[a], Hongtao Liu[a], Haiyan Wang[a,d,*], Yougen Tang[a,*]

[a] Hunan Provincial Key Laboratory of Chemical Power Sources, College of Chemistry and Chemical Engineering, Central South University, Changsha 410083, China
[b] Eco-materials and Renewable Energy Research Center (ERERC), National Laboratory of Solid State Microstructures, Collaborative Innovation Center of Advanced Microstructures, School of Physics, Nanjing University, Nanjing 210093, China
[c] Institute of Materials Science and Devices, Suzhou University of Science and Technology, Suzhou 215011, China
[d] Key Laboratory of Preparation and Application of Environmental Friendly Materials of Ministry of Education, Jilin Normal University, Changchun 130103, China

ARTICLE INFO

Article history:
Received 14 November 2020
Received in revised form 28 December 2020
Accepted 29 December 2020
Available online 15 January 2021

Keywords:
Cu/Cu_2O
Oxygen reduction reaction
Al-air battery
Stability
Synergistic effect

ABSTRACT

Developing high-efficiency, inexpensive, and steady non-precious metal oxygen reduction reaction (ORR) catalysts to displace Pt-based catalysts is significant for commercial applications of Al-air battery. Here, we have prepared the Cu/Cu_2O-NC catalyst with excellent ORR performance and high stability, due to the synergistic effect of Cu and Cu_2O nanoparticles. The half-wave potential (0.8 V) and the limiting-current density (5.20 mA/cm^2) of the Cu/Cu_2O-NC are very close to those of the 20% Pt/C catalyst (0.82 V, 5.10 mA/cm^2). Besides, it exhibits excellent performance with a maximal power density of 250 mW/cm^2 and a stable continuous discharge for more than 90 h in the Al-air battery test. The promoting effects of Cu_2O towards Cu-based ORR catalysts are illustrated as follows: (i) Cu_2O is the major ORR active site by the redox of Cu(II)/Cu(I), which provides excellent ORR activities; (ii) Cu can stabilize the location of Cu_2O by assisting the electron transfer to Cu(II)/Cu(I) redox, which is conducive to the high stability of the catalyst. This work provides a useful strategy for enhancing the ORR performance of Cu-based catalysts.

At present, the growing environmental pollution and energy crisis have prompted people to seek new environmentally friendly energy systems to replace fossil fuels, such as wind energy [1], varieties of clean energy storage technologies [2–6]. Among them, metal-air batteries are catching many eyes due to low cost, environmental friendliness, and high energy density [7,8]. However, their electrochemical performance is restricted by the sluggish kinetics of oxygen reduction reaction (ORR) [9–11]. Nowadays, Pt-based materials are known as the best commercial ORR catalysts, whereas the high value and the low tolerance of Pt become one of the major bottlenecks impeding their further commercial applications [12,13]. Therefore, it is vital to explore inexpensive, high activity, and stable oxygen reduction catalyst [14].

Transition metal-based ORR catalysts have been intensively investigated due to abundant resources, high stability, and outstanding catalytic activity, which may replace the popularly commercial 20% Pt/C and become one of the desirable catalysts for ORR [15–17]. It is known to all that metallic copper has a good electron conductivity property, and it can effectively increase the electron conductivity of the electrocatalysts [18–22]. Cu is often used to form the alloy with Pt, which can further improve the oxygen reduction catalytic performance of the catalyst while reducing the platinum content of Pt-based materials [23,24]. Cu oxides have the potential to become suitable oxygen reduction catalyst due to its variable oxidation states, stronger O_2 adsorption [25–27]. Shim *et al.* reported that silver-copper oxide (Ag@CuO) nano-particles exhibited more ORR catalytic activity than AgNPs or CuO and satisfactory methanol tolerance in alkaline media [28]. Zhang *et al.* investigated the shape dependence of Cu_2O toward ORR activity by synthesizing three different microstructural Cu_2O (spheres, octahedrons, and truncated octahedrons) [29]. It was found that Cu_2O with truncated octahedron shape showed better

---

* Corresponding authors at: Hunan Provincial Key Laboratory of Chemical Power Sources, College of Chemistry and Chemical Engineering, Central South University, Changsha 410083, China.
E-mail addresses: wanghy419@csu.edu.cn (H. Wang), ygtang@csu.edu.cn (Y. Tang).

https://doi.org/10.1016/j.cclet.2021.01.022
1001-8417/

ORR catalytic performance than spheres and octahedron shapes. Li group prepared an n-type Cu_2O doped activated carbon [30], which exhibited a better exchange current density of 1.03 mA/cm^2, 67% higher than the control sample. The outstanding ORR catalytic performance was put down to oxygen vacancies of the n-type Cu_2O, and cubic Cu_2O crystals exclusively expose (111) planes asactive sites.

However, the ORR performances of Cu_2O are limited by poor dispersibility and low conductivity. Aimed at these disadvantages, researchers composite Cu_2O with various carbon materials (graphene or N-doped carbon), due to their good pore structure and large specific surface area [31–34]. A recent report demonstrated that proper catalyst support was critical to the electrochemical performance and durability of the catalyst [35]. Saianand *et al.* dispersed Cu/Cu_2O species onto mesoporous fullerene uniformly, the excellent ORR activity of this compound could benefit from rapid mass transfer and abundant active sites [35]. A Cu@Cu_2O core-shell catalyst was derived from the reduction of Cu(II)-MOF with sodium borohydride solution. The superior ORR activity of it rooted in the special core-shell structure [36].

In this work, the copper phthalocyanine (CuPc) as the copper resource was mixed with ZIF-8 to obtained the Cu-ZIF-8 precursors. Then, the precursors were pyrolyzed to produce Cu/Cu_2O-NC catalyst. It displays excellent ORR activity with high half-wave potential (0.80 V) and limiting current density (5.20 mA/cm^2). Moreover, the Al-air battery with Cu/Cu_2O-NC catalyst shows a supreme power density of 250 mW/cm^2 and excellent discharge stability (maintained 90 h at 1.5 V in 50 mA/cm^2). These results demonstrated that Cu and Cu_2O nanoparticles could synergistically promote the kinetic of ORR to expand the application of Al-air battery.

In a typical method [37], 2.35 g of 2-methylimidazole and X mg (X = 8, 16, 20, 24, 26) of phthalocyanine copper (CuPc) were dispersed into 40 mL methanol, denoted as A, and 40 mL methanol dissolved 1.07 g of $Zn(NO_3)_2·6H_2O$ was denoted as B. The B was poured into the A, then the suspension was stirred at 30 °C for 24 h. The blue powders were obtained by centrifuging and dried in a drying oven at 80 °C for 12 h. At last, they were carbonized at 900 °C for 3 h under flowing nitrogen to obtain the Cu/Cu_2O-NC-X (X = 8, 16, 20, 24, 26) samples.

The synthesis of the Cu-NC sample was similar to that described above for Cu/Cu_2O-NC-X, except 10% Ar/H_2 instead of N_2. Cu/Cu_2O-NC-S sample was obtained by dispersing Cu/Cu_2O-NC into 0.5 mol/L H_2SO_4 solution under stirring for 24 h at 80 °C. The synthesis of the NC sample was similar to that of Cu/Cu_2O-NC-X without CuPc.

The composition of catalysts was tested by X-ray diffraction (XRD) for crystal structure analysis. The composition and chemical states of catalysts were characterized using X-ray photoelectron spectroscopy (XPS, K-Alpha1063, Thermo Scientific) with monochromatized Al Kα excitation. The morphology and microstructure of materials were tested using the scanning electron microscope (SEM, 1002789S FEI Electron Optics B.V) and transmission electron microscope (TEM, FEI Tecnai G2 F20 S-TWLX) equipped with scan TEM (STEM). N_2 adsorption – desorption isotherms were tested by the surface area analyzer (Builder SSA-4200) to evaluate the Brunauer-Emmett-Teller (BET) specific surface areas, pore-volume, and pore diameter distribution.

The three-electrode system on an electrochemical workstation (CHI 760E) was used to test the electrochemical performance of samples. Saturated calomel electrode (SCE) and a Pt wire electrode were used as a reference electrode and counter electrode, respectively. Rotating disk electrode (RDE) endowed with catalyst ink is the working electrode, which was prepared as follows: 6 mg of the catalyst was spread into a mix solution of 950 μL ethanol and 50 μL Nafion (5 wt%), which was dispersed by ultrasound into a uniform ink. Where after 10 μL of ink was dropped onto a glassy carbon electrode with an area of 0.196 cm^2 (the diameter is 5.0 mm), and the weight of the catalyst was ~0.306 mg/cm^2. The ORR performance of as-prepared samples was evaluated by linear sweep voltammetry (LSV) and cyclic voltammetry (CV) in O_2-saturated 0.1 mol/L KOH solutions at room temperature, and all measured potentials are converted to a reversible hydrogen electrode (RHE).

Based on the Koutecky – Levich equation, the number of electrons transferred (n) was calculated:

$$\frac{1}{J}=\frac{1}{J_L}+\frac{1}{J_K}=\frac{1}{B\omega^{1/2}}+\frac{1}{J_K} \tag{1}$$

$$B=0.62nFC_0(D_0)^{2/3}\nu^{-1/6} \tag{2}$$

$$J_{\mathrm{k}}=\frac{J\times J_L}{J_L-J} \tag{3}$$

In which J is the measured current density, J_k and J_L are the kinetic and diffusion-limiting current densities, ω is the electrode rotation rate, F is Faraday's constant, C_0 is the bulk concentration of O_2, D_0 is the diffusion coefficient of O_2, and ν is the kinematic viscosity of the electrolyte.

The application performances of as-prepared catalysts in the Al-air battery made by ourselves were investigated on a Neware battery testing system. The Al-air battery is composed of the anode (Al alloy plate), air cathode (designed active surface area is 3 cm^2 per face and the load is 4.08 mg/cm^2), and alkaline aqueous electrolyte (6 mol/L KOH) with certain inhibitors (0.01 mol/L Na_2SnO_3, 0.0005 mol/L $In(OH)_3$, and 0.0075 mol/L ZnO) [14,38–40].

The air cathode consists of a catalyst layer, a current collector, and a gas diffusion layer. Here, the catalyst layer is made of the catalyst powder mixed with KB, super-P (conductive carbon black), and binder (polytetrafluoroethylene) uniformly in a weight ratio of 3:3:1:3 and was rolled until the thickness is ~ 0.02 cm [41].

ZIF-8 and their derivates/composites, such as Fc@ZIF-8 [42], Co-N_x/C NRA [43], have been investigated as ORR catalysts. Nevertheless, ZIF-8 and Cu-based composites have rarely been reported. In this work, both Cu/Cu_2O-NC and Cu-NC composites are fabricated by the introduction of CuPc into ZIF-8 and subsequent pyrolysis process under N_2 and 10% Ar/H_2 protective atmosphere, respectively, as can be seen from Scheme 1.

The morphologies of the as-prepared NC, Cu-NC and Cu/Cu_2O-NC catalysts were characterized by scanning electron microscope (SEM) and transmission electron microscopy (TEM). In Fig. 1a, the NC catalyst obtained by high-temperature carbonization of ZIF-8 showed the shape of a regular diamond dodecahedron. The microstructure of the Cu-ZIF-8 precursor (Fig. 1b inset) was similar to ZIF-8, indicating that CuPc was dispersed in the ZIF-8 uniformly and its addition could not change the morphology of ZIF-8. The SEM images of Cu-NC and Cu/Cu_2O-NC are shown in Figs. 1b and c. After calcination, the microstructure of Cu-NC was well maintained, whereas agglomerated nanoparticles were observed for Cu/

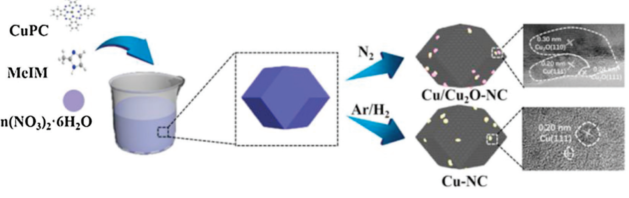

Scheme 1. Synthesis route of the Cu/Cu_2O-NC and Cu-NC catalysts.

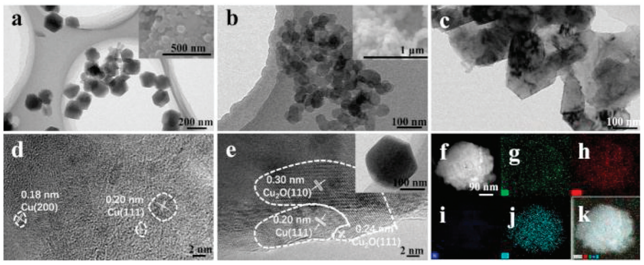

Fig. 1. TEM images of (a) NC and (b) Cu-NC, insets are the SEM images of precursors of corresponding samples. (c)TEM image of Cu/Cu_2O-NC. HRTEM images of (d) Cu-NC and (e) Cu/Cu_2O-NC, inset is the TEM image. (f-k) HAADF-STEM and element mapping images of Cu/Cu_2O-NC.

Cu_2O-NC. From the high-resolution TEM (HRTEM) image of Cu/Cu_2O-NC (Fig. 1e and Fig. S1a in Supporting information), Cu and Cu_2O nanoparticles are neighboring and distributed in the carbon layer, wherein the lattice distances of 0.20 nm, 0.30 nm and 0.24 nm are corresponding to (111) plane of Cu, (110) and (111) plane of Cu_2O particles, respectively [44,45]. According to the HAADF-STEM images (Figs. 1f-k), the Cu element is uniformly dispersed in the carbon layer.

X-ray diffraction (XRD) was applied to characterize the structure of the obtained catalysts. As shown in Fig. 2, only a broad peak of 26.1°, corresponding to the (002) facet of graphite, was observed for the NC sample, indicating that Zn ions were completely removed after pyrolyzing. When CuPc was in-situ introduced into ZIF-8, the as-prepared product was Cu/Cu_2O-NC. It shows that three peaks at 43.3°, 50.4° and 74.1° belong to the cubic phase of Cu (Fm-3m; PDF#04-0836), and three peaks at 36.4°, 42.3°, 61.3° are assigned to Cu_2O (Pn-3m; PDF#05-0667). This result reveals that Cu(II) ions could be reduced to metal Cu and Cu_2O nanoparticles during the pyrolysis process. To study the role of Cu-based nanoparticles in Cu/Cu_2O-NC catalyst, an acid leaching strategy was carried out to remove Cu-based nanoparticles. In the XRD pattern of Cu/Cu_2O-NC-S (Fig. S1b in Supporting information), the peaks of Cu-based nanoparticles are disappeared, and the Cu 2p XPS peaks are very weak in Fig. 3c, indicating the complete removal of metal Cu and Cu_2O nanoparticles. To verify further the role of metal Cu and Cu_2O nanoparticles, a protective atmosphere of 10% Ar/H_2 was used during the pyrolysis to reduce Cu_2O nanoparticles completely. In Fig. 2, the Cu-NC only displays the stronger peaks of metal Cu, meaning that Cu_2O species are disappeared. The HRTEM images of Cu-NC (Fig. 1d) displays the (200) and (111) planes of metallic Cu and manifest that Cu nanoparticles are uniformly embedded in the carbon layer. Namely, all Cu(II) ions in the Cu-ZIF-8 were reduced to metal Cu nanoparticles under Ar/H_2. In Fig. 3b, although the high-resolution Cu 2p spectrum of Cu-NC shows similar results with that of Cu/Cu_2O-NC, the area ratio of Cu/Cu(II) in Cu-NC is 1.55, which is higher than that of Cu/Cu_2O-NC (0.5) in Fig. 3a. It means that the Cu/Cu_2O-NC has a higher Cu_2O content than the Cu-NC [46].

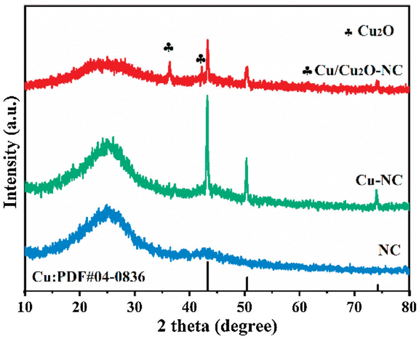

Fig. 2. XRD patterns of Cu-NC, Cu/Cu_2O-NC, NC.

The XPS survey spectra (Fig. S2a in Supporting information) of Cu/Cu_2O-NC, Cu-NC and Cu/Cu_2O-NC-S shows obvious peaks of C 1s, N 1s and O 1s, respectively. Atomic concentrations of elements in catalysts is shown in Table 1. Note that the concentration of Cu in these catalysts is very low, so the peaks of Cu are not identified clearly. The XPS high-resolution Cu 2p spectrum of Cu/Cu_2O-NC in Fig. 3a displays the main two pairs of peaks of 952.4 eV/932.5 eV and 954.7 eV/934.9 eV, which correspond to the Cu $2p_{1/2}$/Cu $2p_{3/2}$ state of Cu and Cu(II), respectively. Meanwhile, the satellite peak of CuO (at 943.0 eV) comes from the oxidation of Cu_2O on the catalyst surface [47]. The high-resolution N 1s spectrum of Cu/Cu_2O-NC, Cu-NC and Cu/Cu_2O-NC-S (Figs. 3d-f) could be divided into four types of N species: pyridinic N (~398.4 eV), pyrrolic N (~399.8 eV), graphitic N (~401.0 eV), and oxidized N (~402.7 eV). Table S2 (Supporting information) lists the corresponding contents of different N species for three catalysts, which are calculated from N 1s spectra. Notably, the content of pyridinic N in Cu-NC is significantly higher than other catalysts [48,49]. Therefore, Cu-based sites (Cu and/or Cu_2O) determine the ORR activity of Cu/Cu_2O-NC and Cu-NC. The BET surface area and pore size distribution of the Cu/Cu_2O-NC and other contrast catalysts are shown in Fig. S3 (Supporting information). Obviously, all samples display a high specific surface area, which is mainly attributed to the N-doped carbon. Because Cu and Cu_2O nanoparticles will block the pores of the N-doped carbon support, the specific surface area of Cu/Cu_2O-NC (604.14 m^2/g) is inferior to Cu-NC (971.26 m^2/g) and NC (711.36 m^2/g) [3].

The ORR activity of the Cu/Cu_2O-NC and other contrast samples was evaluated by rotating disk electrode (RDE) measurements with 1600 rpm in O_2-saturated 0.1 mol/L KOH at a sweep rate of 10 mV/s. As shown in Fig. 4a, the NC sample exhibits poor oxygen reduction activity, indicating the N-doped carbon is not the major ORR active site. When CuPc was introduced into ZIF-8, the obtained Cu/Cu_2O-NC catalyst demonstrates significantly enhanced catalytic activity towards ORR. Meanwhile, the effect of the added CuPc amount on ORR catalytic performance was also investigated (Fig. S4 in Supporting information). When 24 mg CuPc was added to the ZIF-8 precursor, the resultant Cu/Cu_2O-NC catalyst exhibits the best ORR catalytic performance. The half-wave potential ($E_{1/2}$) of Cu/Cu_2O-NC is about 0.80 V, closing to that of commercial 20% Pt/C catalyst, and the limiting current density is 5.20 mA/cm^2, even exceeding that of commercial 20% Pt/C catalyst (5.10 mA/cm^2). Besides, the Cu-NC catalyst contains the highest content of pyridine N with high oxygen reduction activity, but shows inferior ORR activities ($E_{1/2}$ = 0.78 V, 4.08 mA/cm^2) compared to Cu/Cu_2O-NC. This fact proves that N-doped carbon is not the activity-determining species and the presence of Cu_2O in the catalyst avails the ORR catalytic activity due to the superior absorption to the oxygen [50]. Furthermore, after acid pickling, a little of Cu-based species are left in the Cu/Cu_2O-NC-S catalyst, which performs comparable ORR activities of NC catalyst. The result means that Cu and Cu_2Ospecies are equally important in boosting ORR activity and constitute the active sites of Cu/Cu_2O-NC. The CV curves of as-prepared catalysts are shown in Fig. 4b. Clearly, the ORR peak potential of Cu/Cu_2O-NC (0.82 V) is higher than that of Cu-NC (0.80 V), Cu/Cu_2O-NC-S (0.79 V) and NC (0.75 V) catalysts. This result also supports that the superior ORR activities of Cu/Cu_2O-NC are attributed to both Cu and Cu_2O nanoparticles. Besides, the peaks of Cu-NC and Cu/Cu_2O-NC in 0.6 V are assigned to the reaction process of Cu(I) and Cu(II) [36].

The Koutecky-Levich (K-L) plots of Cu/Cu_2O-NC (Fig. 4c) and Cu-NC (Fig. S5 in Supporting information) were obtained by fitting the LSV curves at various rotating rates. The current density of Cu/Cu_2O-

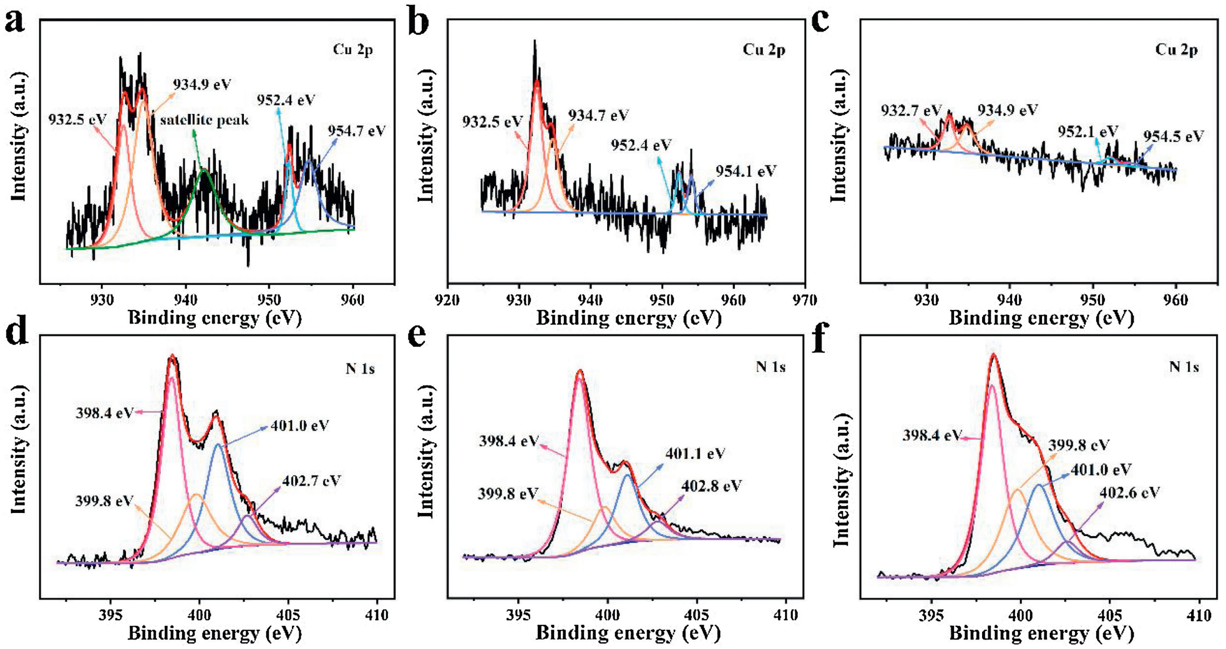

Fig. 3. Cu 2p XPS spectra of (a) Cu/Cu_2O-NC, (b) Cu-NC and (c) Cu/Cu_2O-NC-S. N 1s XPS spectra of (d) Cu/Cu_2O-NC, (e) Cu-NC and (f) Cu/Cu_2O-NC-S.

Table 1
Atomic concentrations proportions (at%) of elements in as-prepared catalysts determined by XPS.

Catalysts	Composition (at%)			
	C	N	O	Cu
Cu/Cu_2O-NC	87.41	5.88	6.41	0.3
Cu-NC	85.27	8.42	6.06	0.23
Cu/Cu_2O-NC-S	81.6	9.34	8.92	0.14

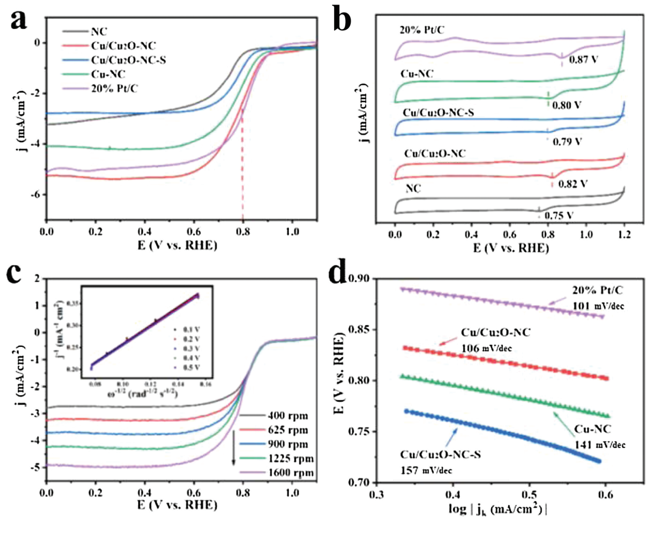

Fig. 4. (a) LSV curves and (b) CV curves of the NC, Cu-NC, Cu/Cu_2O-NC, Cu/Cu_2O-NC-S and the commercial Pt/C catalyst. (c) LSV curves of Cu/Cu_2O-NC at different rotating rates. The inset is the K-L plots of the Cu/Cu_2O-NC at different potentials. (d) Tafel plots of the Cu-NC, Cu/Cu_2O-NC, Cu/Cu_2O-NC-S and the commercial Pt/C catalyst.

NC increases proportionally to the rotation rate, and the K-L curves (inset of Fig. 4c) exhibit an almost parallel linear relationship. LSV curves (Fig. S5a) and K-L plots (Fig. S5b) of Cu-NC show the same characteristics. These facts indicate that the behavior of ORR fitted the first-order reaction kinetics [7,31]. Numbers of electrons transferred calculated by K-L curves of Cu-NC and Cu/Cu_2O-NC are 3.9 and 4, respectively, meaning that the ORR processes of two catalysts both perform as the four-electron transfer process. The ORR kinetics of electrocatalysts are further evaluated by the Tafel slope obtained from the LSV curves calculation based on the Tafel equation. In Fig. 4d, the Tafel slope order of all samples is as follows: 20% Pt/C (101 mV/dec) < Cu/Cu_2O-NC (106 mV/dec) < Cu-NC (141 mV/dec) < Cu/Cu_2O-NC-S (157 mV/dec). This result reveals that the ORR kinetic of Cu/Cu_2O-NC is comparable to 20% Pt/C, and faster than Cu-NC and Cu/Cu_2O-NC-S. Meanwhile, the kinetic current density (j_k) of Cu/Cu_2O-NC (4.19 mA/cm^2) in Fig. 5a is superior to NC (0.55 mA/cm^2), Cu-NC (2.74 mA/cm^2), and Cu/Cu_2O-NC-S (1.50 mA/cm^2) in 0.8 V, which further proves the excellent kinetic process of Cu/Cu_2O-NC.The ORR kinetics of Cu/Cu_2O-NC should be attributed to the rapid conduction of electrons and the existence of redox reactions of Cu(I) and Cu(II).

Furthermore, Cu/Cu_2O-NC exhibits outstanding ORR catalytic stability throughout *i-t* chronoamperometry response (Fig. 5b) and the accelerated durability test (Fig. 5c). After 10000 s discharging at 0.7 V, the current density of Cu/Cu_2O-NC remains at 86% of the initial current density higher than the 20% Pt/C catalyst (76%) and Cu-NC (71%). In Figs. 5c and d, after the accelerated durability test (ADT), though the decrease of the $E_{1/2}$ for Cu/Cu_2O-NC is similar to 20% Pt/C, the former limiting current density maintains well, compared to the latter. These results highlight the outstanding electrochemical performance and excellent stability of Cu/Cu_2O-NC, which are mainly attributed to good synergistic effect Cu_2O and Cu toward ORR. Among them, Cu(I) (from Cu_2O) has a strong intermediate binding energy with O species, which can effectively improve the O_2 adsorption capacity of the catalyst during the ORR process [48,51–53]. Cu nanoparticles with high conductivity can donate free electrons to Cu(I) easily [54]. In addition, the N-doped carbon can provide Cu/Cu_2O-NC catalyst with the high specific surface area, which expose more active sites to the three-phase reaction interface, effectively improving the ORR catalytic performance.

The practical performance of the Cu/Cu_2O-NC catalyst in a home-made Al-air battery system was evaluated, and its scheme is

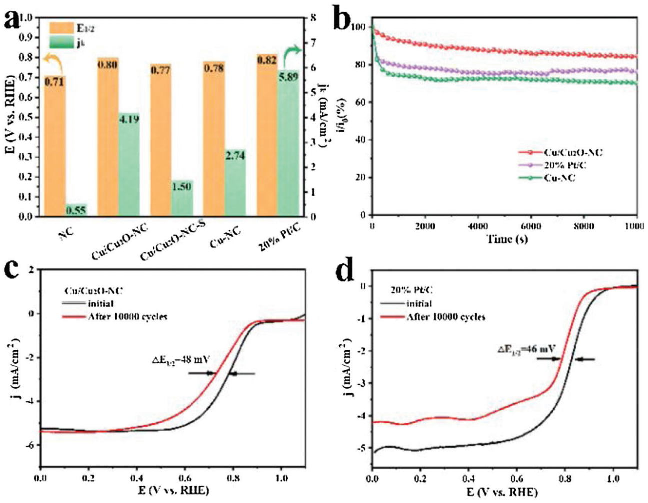

Fig. 5. (a) The comparison of j_k at 0.8 V and $E_{1/2}$ for different catalysts. (b) *i-t* chronoamperometry response of Cu/Cu_2O-NC, Cu-NC and the commercial 20% Pt/C catalyst at 0.7 V at a rotating rate of 1600 rpm. LSV curves of (c) Cu/Cu_2O-NC and (d) the commercial 20% Pt/C catalyst before and after ADT. The ADT was evaluated by scan 10000 CV cycles at a sweep rate of 200 mV/s.

shown in Fig. S6 (Supporting information). At the same time, Figs. 6a and b show the power density and discharge voltage at different discharge current densities of Cu/Cu_2O-NC and Cu-NC, respectively. With the discharge current density increase, the power density curve of Cu/Cu_2O-NC shows a steady upward trend until the discharge current density exceeds 270 mA/cm^2 achieving a maximal power density of 250 mW/cm^2. While Cu-NC only delivers a maximum power density of less than 200 mW/cm^2 during the discharge current density of 190 mA/cm^2. Compared to Cu-NC, the better practical performance of Cu/Cu_2O-NC should be derived from the promoting effect of Cu_2O nanoparticles.

The discharge curves of Cu-NC and Cu/Cu_2O-NC catalysts were tested at 50, 100 and 200 mA/cm^2 for 100 min, respectively. As seen in Fig. 6c, both samples display almost the same discharge voltages closing to 1.5 V at 50 mA/cm^2. Nevertheless, with the current density increases, the gap of discharge voltage between Cu/Cu_2O-NC and Cu-NC grows larger and larger. At 200 mA/cm^2, the discharge voltage of Cu/Cu_2O-NC reaches 1.1 V, nearly 100 mV higher than that of Cu-NC. The excellent discharge performance of Cu/Cu_2O-NC at a large current density benefit from the synergistic effect of Cu and Cu_2O, which provides more ORR active sites and remarkable electron conduction capability. Hence, the performance of the two catalysts gradually comes into being a large gap, as the discharge current density increases.

We further evaluated the stability of the oxygen reduction catalyst by the long-term discharge of the Al-air battery. In Fig. 6d, the Al-air battery with Cu/Cu_2O-NC catalyst has a continuous discharge time of up to 90 h, and the average voltage is maintained at about 1.5 V at a discharge current density of 50 mA/cm^2. The fluctuation of the discharge curve only occurs when the aluminum anode and the electrolyte are refueled. For Cu-NC, the averaged discharge voltage is 1.48 V, and the discharge time is only 70 h (Fig. S7 in Supporting information), indicating that the stability of Cu/Cu_2O-NC catalyst is superior to Cu-NC in practical application.

The excellent ORR performances of the Cu/Cu_2O-NC catalyst benefited from the synergistic effect of the Cu and Cu_2O nanoparticles. To determine the mechanism of synergistic effect, DFT calculations was applied to carry out the thermodynamics of ORR process for Cu site and Cu_2O site, the calculation details was described in Supporting information. According to the HRTEM of Cu/Cu_2O-NC catalyst, Cu (111) facet and Cu_2O (110) facet were chosen as the objects for all calculations. Fig. S8 (Supporting information) provides the models of the O_2 adsorption at Cu (111) facet and Cu_2O (110) facet. The calculation results (Table S3 in Supporting information) prove that the O_2 adsorption energy of Cu_2O (110) facet (-1.62 eV) is lower than that of Cu (111) facet (-1.21 eV), meaning that the O_2 molecules prefer to adsorbing on the Cu_2O sites. Figs. 7a and b display the free energy plots of ORR process for Cu_2O (110) facet and Cu (111) facet. Note that the calculated onset potential of Cu_2O (110) facet (0.85 V) is higher than that of Cu (111) facet (0.51 V). Such phenomena demonstrate that Cu_2O is the major active sites for ORR. Thus, in the LSV curve of Cu/Cu_2O-NC catalyst, the high onset potential is attributed to Cu_2O site, and the high limited current density is attributed to Cu site due to the high intrinsic electric conductivity of it [55,56].

According to these facts, the possible ORR mechanism on the Cu/Cu_2O composite is presented in Figs. 7c and d, which shows a typical four-electron process in the following: (i) Cu_2O on the surface of Cu/Cu_2O-NC catalyst can easily absorb oxygen in the air to obtain $Cu_2O\cdots O_2$ (Eq. 4) [53]; (ii) the $Cu_2O\cdots O_2$ reacts with H_2O molecules and simultaneously receives an electron to generate

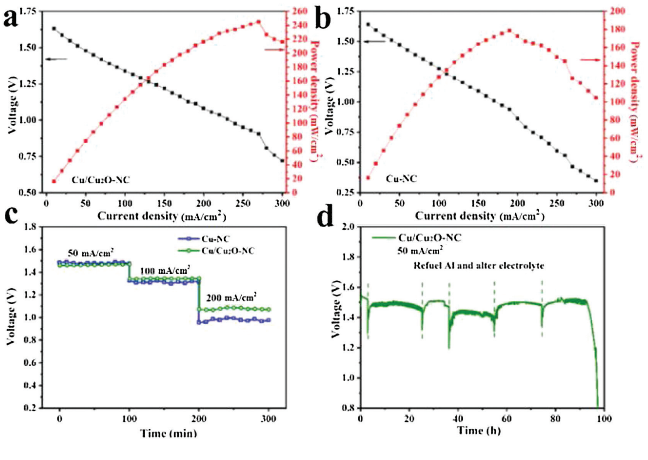

Fig. 6. Power density curves of (a) Cu/Cu_2O-NC and (b) Cu-NC. (c) Discharge curves of Cu-NC and Cu/Cu_2O-NC at different discharge current density. (d) Long-term discharge curves of the Cu/Cu_2O-NC at 50 mA/cm^2. All tests are finished in Al-air batteries.

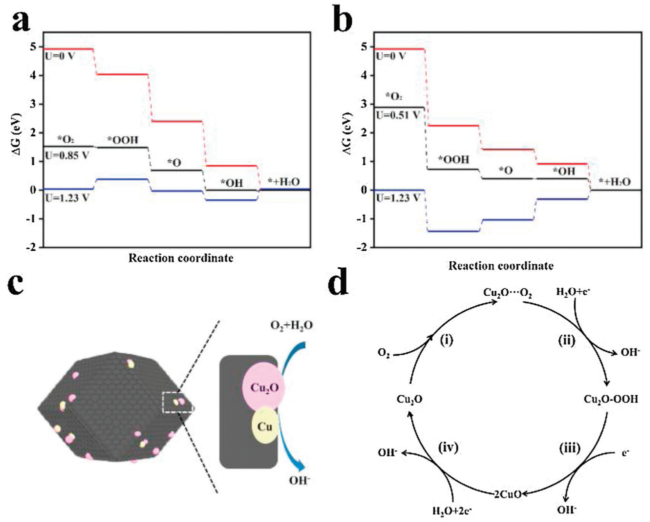

Fig. 7. The free energy plots of ORR process for (a) Cu_2O (110) facet and (b) Cu (111) facet. (c, d) ORR mechanism schematic diagram of the Cu/Cu_2O-NC catalyst.

Cu_2O-OOH in an alkaline environment (Eq. 5); (iii) The Cu_2O-OOH is unstable and easily loses OH^- to form CuO when it captures an electron (Eq. 6); (iv) CuO is reduced to Cu_2O by the electrons from the catalyst (Eq. 7). Thus, Cu_2O is regarded as the major active site, in which the efficient Cu(II)/Cu(I) redox for ORR can provide high ORR activity for Cu/Cu_2O-NC catalyst [46,57].

$$Cu_2O + O_2 \rightarrow Cu_2O \cdots O_2 \quad (4)$$

$$Cu_2O \cdots O_2 + H_2O + e^- \rightarrow Cu_2O - OOH + OH^- \quad (5)$$

$$Cu_2O - OOH + e^- \rightarrow 2CuO + OH^- \quad (6)$$

$$2CuO + H_2O + 2e^- \rightarrow Cu_2O + 2OH^- \quad (7)$$

Meanwhile, Cu nanoparticles on Cu/Cu_2O-NC catalyst act as a good conductor of electrons, and maintain the electron support for Cu_2O [54]. More importantly, the reduction reaction of Cu(II) prefers to occur at the surface of Cu, indicating that the Cu nanoparticles can catch the Cu_2O active sites and decrease the loss of Cu_2O during the ORR process. Benefited by the synergistic effect of Cu and Cu_2O, Cu/Cu_2O-NC could catalyze the ORR like other excellent catalysts. Up to now, the Cu/Cu_2O-NC catalyst is one of the best Cu-based ORR catalysts under both electrochemical and practical tests, as summarized in Table S4. This study furnishes an innovative strategy for promoting the ORR activities of Cu-based catalysts.

In summary, we prepared Cu/Cu_2O-NC catalyst with the $E_{1/2}$ of 0.8 V and J_L of 5.20 mA/cm^2, which are close to the Pt/C. Interestingly, the durability of Cu/Cu_2O-NC is superior to the Pt/C catalyst. After a comparative study with the Cu-NC catalyst, it is found that the Cu_2O active site plays a major role in enhancing the ORR activity in Cu/Cu_2O-NC due to the efficient Cu(II)/Cu(I) redox. And the Cu nanoparticles can catch the active Cu_2O during the ORR process, facilitating the high stability of Cu/Cu_2O-NC catalyst. Besides, the excellent ORR performances are also presented in the Al-air battery application with a high power density (250 mW/cm^2) and high discharge stability (maintained 90 h at 1.5 V in 50 mA/cm^2). This work provides a high-activity and practical Cu/Cu_2O-NC catalyst and reports a useful strategy to improve the ORR performances for Cu-based catalysts.

Declaration of competing interest

The authors declare that they have no known competing financial interests or personal relationships that could have appeared to influence the work reported in this paper.

Acknowledgments

This research was financially supported by the National Key R&D Program of China (No. 2019YFA0210300), National Nature Science Foundation of China (No. 21671200), Hunan Provincial Science and Technology Plan Project of China (Nos. 2017TP1001, 2018RS3009 and 2019GK2033). H. Wang also thanks for the financial support from The Open Project Program of Key Laboratory of Preparation and Application of Environmental Friendly Materials (No. 2019006), Ministry of Education.

Appendix A. Supplementary data

Supplementary material related to this article can be found, in the online version, at doi:https://doi.org/10.1016/j.cclet.2021.01.022.

References

[1] T. Souxes, I.M. Granitsas, C. Vournas, Electr. Power Syst. Res. 170 (2019) 48–56.
[2] Q. Wang, H. He, J. Luan, et al., Electrochim. Acta 309 (2019) 242–252.
[3] J. Li, J. Chen, H. Wan, et al., Appl. Catal. B: Environ. 242 (2019) 209–217.
[4] N.K. Wagh, S.S. Shinde, C.H. Lee, et al., Appl. Catal. B: Environ. 268 (2020) 118746.
[5] Y. Wang, H. Zhou, Chem. Commun. 46 (2010) 6305–6307.
[6] D. Liu, Y. Du, T. Li, et al., Chem. Commun. 56 (2020) 11465–11468.
[7] J. Li, N. Zhou, J. Song, et al., ACS Sustain. Chem. Eng. 6 (2017) 413–421.
[8] C. Zhu, Q. Shi, B.Z. Xu, et al., Adv. Energy Mater. 8 (2018) 1801956.
[9] M. Mao, J. Deng, T. Yan, et al., ACS Sustain. Chem. Eng. 7 (2019) 19268–19276.
[10] Lp. Wang, J. Tian, Js. Li, et al., J. Cent. South. Univ. 26 (2019) 1458–1468.
[11] J. Li, C. Guo, C.M. Li, ChemSusChem 13 (2020) 1047–1070.
[12] J.C. Li, Z.Q. Yang, D.M. Tang, et al., NPG Asia Mater. 10 (2018) e461.
[13] J.J. Xu, C.H. Xiao, S.J. Ding, Chin. Chem. Lett. 28 (2017) 748–754.
[14] J. Li, J. Chen, H. Wang, et al., Energy Storage Mater. 8 (2017) 49–58.
[15] S. Zheng, X. Li, B. Yan, et al., Adv. Energy Mater. 7 (2017) 1602733.
[16] F. Li, L. Fu, J. Li, et al., J. Electrochem. Soc. 164 (2017) A3595–A3601.
[17] C.X. Zhao, B.Q. Li, J.N. Liu, et al., Chin. Chem. Lett. 30 (2019) 911–914.
[18] F. Li, J. Li, Q. Feng, et al., J. Energy Chem. 27 (2018) 419–425.
[19] H.N. Wang, X. Chen, R. Chen, et al., J. Power Sources 435 (2019) 226766.
[20] J.N. Heo, J. Kim, J.Y. Do, et al., Appl. Catal. B: Environ. 266 (2020) 118648.
[21] N. Guo, H. Xue, A. Bao, et al., Angew. Chem. 59 (2020) 13778–13784.
[22] M. Devaraj, R. Saravanan, R. Deivasigamani, et al., J. Mol. Liq. 221 (2016) 930–941.
[23] L.X. Luo, C.H. Fu, S.Y. Shen, et al., J. Mater. Chem. A 8 (2020) 22389–22400.
[24] M. Gong, D. Xiao, Z. Deng, et al., Appl. Catal. B: Environ. 282 (2021) 119617.
[25] Q. Li, P. Xu, B. Zhang, et al., J. Phys. Chem. C 117 (2013) 13872–13878.
[26] F. Dong, P. Zhang, K. Li, et al., Nanomaterials 6 (2016) 238.
[27] Y. Xu, H. Wang, R. Zhu, et al., Chem. Asian J. 8 (2013) 1120–1127.
[28] H. Im, S. Noh, J.H. Shim, Electrochim. Acta 329 (2020) 135172.
[29] X. Zhang, Z. Yi, H. Huang, et al., New J. Chem. 42 (2017) 458–464.
[30] X. Zhang, K. Li, P. Yan, et al., Bioresour. Technol. 187 (2015) 299–304.
[31] S. Xin, J. Shen, G. Liu, et al., Energy 196 (2020) 117123.
[32] D. Li, T. Liu, Z. Yan, et al., ACS Appl. Mater. Interfaces 12 (2020) 7030–7037.
[33] S. Xin, J. Shen, G. Liu, et al., Chem. Eng. J. 380 (2020) 122446.
[34] R. Zhong, C. Zhi, Y. Wu, et al., Chin. Chem. Lett. 31 (2020) 1588–1592.
[35] G. Saianand, A.I. Gopalan, J.C. Lee, et al., Small (2019) e1903937.
[36] A. Kim, N. Muthuchamy, C. Yoon, et al., Nanomaterials 8 (2018) 138.
[37] R. Jiang, L. Li, T. Sheng, et al., J. Am. Chem. Soc. 140 (2018) 11594–11598.
[38] L. Wang, L. Fu, J. Li, et al., J. Mater. Sci. 53 (2018) 10280–10291.
[39] K. Liu, Z. Peng, H. Wang, et al., J. Electrochem. Soc. 164 (2017) F475–F483.
[40] J. Li, N. Zhou, H. Wang, et al., J. Electrochem. Soc. 162 (2015) A2302–A2307.
[41] D. Liu, J. Tian, Y. Tang, et al., Chem. Eng. J. 406 (2021) 126772.
[42] J. Wang, G. Han, L. Wang, et al., Small 14 (2018) e1704282.
[43] I.S. Amiinu, X. Liu, Z. Pu, et al., Adv. Funct. Mater. 28 (2018) 1704638.
[44] J. Liu, L. Peng, Y. Zhou, et al., ACS Sustain. Chem. Eng. 7 (2019) 15739–15746.
[45] S.M. Majhi, P. Rai, S. Raj, et al., ACS Appl. Mater. Interfaces 6 (2014) 7491–7497.
[46] W. Geng, W. Li, L. Liu, et al., Fuel 259 (2020) 116267.
[47] T. Ghodselahi, M.A. Vesaghi, A. Shafiekhani, et al., Appl. Surf. Sci. 255 (2008) 2730–2734.
[48] H. Shao, X. Zhang, H. Huang, et al., ACS Appl. Mater. Interfaces 9 (2017) 41945–41954.
[49] D. Guo, R. Shibuya, C. Akiba, et al., Science 351 (2016) 361–365.
[50] Q. He, X. Yang, R. He, et al., J. Power Sources 213 (2012) 169–179.
[51] H. Wu, H. Li, X. Zhao, et al., Energy Environ. Sci. 9 (2016) 3736–3745.
[52] Z.J. Zuo, N. Li, S.Z. Liu, et al., Appl. Surf. Sci. 366 (2016) 85–94.
[53] X. Yu, C. Zhao, T. Zhang, et al., Phys. Chem. Chem. Phys. 20 (2018) 20352–20362.
[54] X.L. Chen, L.S. Ma, W.Y. Su, et al., Electrochim. Acta 331 (2020) 135273.
[55] M. Bajdich, M. Garcia-Mota, A. Vojvodic, et al., J. Am. Chem. Soc. 135 (2013) 13521–13530.
[56] H.A. Hansen, J. Rossmeisl, J.K. Nrskov, Phys. Chem. Chem. Phys. 10 (2008) 3722–3730.
[57] P. Liu, X. Liu, F. Dong, et al., Sci. Total Environ. 631–632 (2018) 849–856.